Draft version June 9, 2026
Typeset using LaTeX **twocolumn** style in AASTeX7.0.1

A Scaling Relation of LRDs between Broad Hα and Bolometric Luminosities: Enhanced Broad Hα Emission Relative to Low-z Type 1 AGN

Hiroto Yanagisawa [1,2] Masami Ouchi [3,1,4,5] Tomokazu Kiyota [3,4] Yuta Kageura [1,2] Makoto Ando [1] Yuichi Harikane [1] Minami Nakane [1,2] Yoshiaki Ono [1] and Yui Takeda [3,4]

[1] *Institute for Cosmic Ray Research, The University of Tokyo, 5-1-5 Kashiwanoha, Kashiwa, Chiba 277-8582, Japan*
[2] *Department of Physics, Graduate School of Science, The University of Tokyo, 7-3-1 Hongo, Bunkyo, Tokyo 113-0033, Japan*
[3] *National Astronomical Observatory of Japan, 2-21-1 Osawa, Mitaka, Tokyo 181-8588, Japan*
[4] *Astronomical Science Program, Graduate Institute for Advanced Studies, SOKENDAI, 2-21-1 Osawa, Mitaka, Tokyo 181-8588, Japan*
[5] *Kavli Institute for the Physics and Mathematics of the Universe (WPI), The University of Tokyo, 5-1-5 Kashiwanoha, Kashiwa, Chiba 277-8583, Japan*

ABSTRACT

We investigate the demography of little red dots (LRDs) using 37 objects at $z \sim 3$–7 with JWST/NIRSpec PRISM and grating spectra compiled from various JWST programs. We focus on spectroscopic quantities of the broad Hα luminosity $L_{\mathrm{H}\alpha,\mathrm{broad}}$ (and the broad Hβ luminosity $L_{\mathrm{H}\beta,\mathrm{broad}}$ where available) and the bolometric luminosity L_{bol} represented by modified blackbody emission, avoiding quantities contaminated by host-galaxy emission (e.g., total Hα luminosity). We identifiy a tight scaling relation between $L_{\mathrm{H}\alpha,\mathrm{broad}}$ and L_{bol}, supporting the interpretation that these emissions are primarily powered by the central engine. Interestingly, the $L_{\mathrm{H}\alpha,\mathrm{broad}}$–$L_{\mathrm{bol}}$ scaling relation of LRDs is enhanced by a factor of ~ 40 in $L_{\mathrm{H}\alpha,\mathrm{broad}}$ relative to that of low-z Type 1 AGN. A similar trend is found in the $L_{\mathrm{H}\beta,\mathrm{broad}}$–$L_{\mathrm{bol}}$ relation, although the enhancement in $L_{\mathrm{H}\beta,\mathrm{broad}}$ is smaller, only by a factor of ~ 10. We explore the physical origin of these enhancements and find that Cloudy photoionization modeling within the classic locally optimally-emitting cloud (LOC) framework can explain them through an increase in the covering factor from $\sim 20\%$ (Type 1 AGN) to $\sim 100\%$ (LRDs), together with an increase in the hydrogen column density from $N_{\mathrm{H}} \sim 10^{23}\,\mathrm{cm}^{-2}$ to $\gtrsim 10^{24}\,\mathrm{cm}^{-2}$, with a preferred gas density of $\sim 10^{10}\,\mathrm{cm}^{-3}$, successfully reproducing the modified blackbody emission. Such a nearly unity covering factor without requiring a gas density increase may result from a significant increase in the BLR filling factor or size, corresponding to a "stuffed BLR" or "giant BLR," respectively.

1. INTRODUCTION

Recent James Webb Space Telescope (JWST) spectroscopy has revealed a population of compact, broad-line AGN candidates at $z \gtrsim 3$ whose rest-frame UV–optical spectra show a characteristic "V-shaped" SED: a blue UV continuum combined with a red optical continuum and often a prominent Balmer break (e.g., D. D. Kocevski et al. 2023; Y. Harikane et al. 2023; J. Matthee et al. 2024; J. E. Greene et al. 2024; R. Maiolino et al. 2024; T. S. Tanaka et al. 2025; K. Inayoshi & L. C. Ho 2025). These sources, commonly referred to as little red dots (LRDs), typically show unusually weak X-ray, mid-infrared, and radio emission compared to expectations from classical unobscured AGN, complicating their identification and physical interpretation (M. Yue et al. 2024; T. T. Ananna et al. 2024; H. B. Akins et al. 2025; A. J. Gloudemans et al. 2025; R. Maiolino et al. 2025). The combination of broad Balmer emission and anomalous multi-wavelength properties has motivated scenarios in which the central engine is embedded in optically thick gas (an envelope/cocoon) that can both reprocess the intrinsic emission into a quasi-thermal optical continuum and alter the observed line/continuum ratios (K. Inayoshi & R. Maiolino 2025; K. Inayoshi et al. 2025; D. Kido et al. 2025).

Establishing robust empirical relations among observables is essential for testing whether LRDs are powered primarily by accreting black holes and, if so, how their line-emitting regions differ from the broad-line regions (BLRs) of type 1 AGN. In classical AGN, broad Balmer-line luminosities correlate tightly with the optical continuum and with bolometric luminosity, and these relations are widely used as practical calibrations linking recombination-line emission to the ionizing continuum and BLR physics (e.g., J. E. Greene & L. C. Ho 2005;

Email: yana@icrr.u-tokyo.ac.jp

J. Stern & A. Laor 2012; Y. Shen & X. Liu 2012). If LRDs share the same underlying central engine mechanism, one might expect them to follow similar scaling relations. Conversely, any systematic deviation from the AGN relations would provide direct, quantitative evidence that LRDs have distinct BLR conditions and/or continuum reprocessing.

The total (i.e., narrow+broad) Balmer-line luminosities can be significantly affected by host-galaxy emission and narrow-line region contamination, and the limited spectral resolution of JWST/NIRSpec PRISM alone can make decomposition of narrow and broad components uncertain. To isolate the BLR contribution and minimize systematics, it is crucial to measure the luminosity of the broad component using spectra with sufficient resolution. In this paper, we use publicly available JWST/NIRSpec observations to construct a large spectroscopic sample of LRDs with broad Hα emission over $z \sim 3$–7, combining PRISM spectra with medium- and high-resolution grating data to robustly separate narrow and broad line emission. We then ask two closely related questions: (1) does the long-established AGN $L_{\mathrm{H}\alpha,\mathrm{broad}}$–$L_{\mathrm{bol}}$ scaling relation also hold for LRDs, and (2) if so, is it consistent in normalization with type 1 AGN? In Section 2, we describe the sample construction and data sets. In Section 3, we detail our spectral fitting and continuum characterization procedures. Section 4 presents the resulting scaling relations and comparison with previous studies. Section 5 discusses their implications. We summarize our main conclusions in Section 6. Throughout this paper, we assume cosmology parameters based on the TT, TE, EE + lowE + lensing + BAO result from Planck Collaboration et al. (2020) with $H_0 = 67.66\,\mathrm{km\,s^{-1}\,Mpc^{-1}}$, $\Omega_{\mathrm{m}} = 0.30966$, and $\Omega_{\mathrm{b}} = 0.04897$.

2. SAMPLE AND DATA

2.1. *DJA Sample*

We use the publicly available JWST/NIRSpec spectra from the Dawn JWST Archive (DJA; K. E. Heintz et al. 2024; A. de Graaff et al. 2025a; F. Valentino et al. 2025) version 4.4[1]. We start from sources with redshift quality grade 3, and require that a PRISM spectrum is available. To enable consistent emission-line measurements across the sample, we further impose that Hα and [O III]λ5007 are have peak signal-to-noise ratio (SNR) of SNR > 5 in at least one of the NIRSpec medium ($R \sim 1000$) or high ($R \sim 2700$) resolution gratings provided in DJA for each target. The [O III] λ5007 emission line is used to verify that any outflow-related component has negligible influence on the luminosity measurements of the broad Balmer lines originating from the BLR of LRDs. We then search for broad Hα emission among the selected targets. We perform a double-Gaussian fit consisting of a narrow and a broad component to Hα. We require the broad component has FWHM = 700–6000 $\mathrm{km\,s^{-1}}$ and $\mathrm{SNR_{broad}} > 5.0$. The upper limit on the FWHM is imposed because nearly all targets with FWHM $> 6000\,\mathrm{km\,s^{-1}}$ do not exhibit a genuine broad Hα component; instead, their continua are effectively reproduced by extremely broad Gaussian profiles. After visually inspecting the fitting results, we identify 59 objects that show broad Hα emission.

We further assess the compactness of these objects using NIRCam F444W imaging from the DJA mosaics (version 7[2]; F. Valentino et al. 2023). Five objects lie outside the NIRCam F444W coverage, which are therefore excluded from the subsequent analysis. Aperture photometry is performed using circular apertures with diameters of 0.4″ and 0.2″. We adopt the following compactness criterion:

$$f_{\mathrm{F444W}}(0.4'')/f_{\mathrm{F444W}}(0.2'') < 1.7, \quad (1)$$

as employed in e.g., I. Labbe et al. (2025) and J. E. Greene et al. (2024). Here, f_{F444W} denotes the F444W flux measured within the specified aperture diameter. We find that only two objects do not satisfy this compactness requirement. We thus exclude these from the sample, resulting in a final set of 52 objects.

2.2. *NIRSpec/IFU Sample*

In addition to the DJA sample, we include an NIRSpec/IFU sample drawn from the programs GO 5665 (PI: Matthee) and GO 5015 (BlackTHUNDER; PI: Übler and Maiolino), comprising 8 LRDs and 2 type 1 AGNs. Among these 10, two targets, 159717 and GS-13971, are also selected in DJA sample. Because IFU data have higher SNR, we use IFU data and exclude DJA data for these two objects.

The JWST/NIRSpec IFU data were reduced from the Level-1b uncalibrated products retrieved from MAST. We processed the data with the JWST Calibration Pipeline (v2.0.1) using the CRDS context `jwst_1535.pmap`. For each exposure, we ran the standard Detector1 and Spec2stages to produce count-rate images and calibrated two-dimensional products. We then constructed median-stacked data cubes and corresponding noise cubes from the reduced individual expo-

[1] https://zenodo.org/records/15472354

[2] https://dawn-cph.github.io/dja/imaging/summary/

sures. The resulting spaxel scale was 0.″1. The noise cubes were estimated from the scatter among the contributing frames, scaled by the square root of the number of exposures. The median stacking procedure is described in T. Kiyota et al. (2025) in detail.

One-dimensional spectra were extracted from the median-stacked IFU cubes. For each target, the extraction aperture was centered on the source position identified from the Hα narrowband map, starting from the catalog coordinates and allowing a local centroid refinement. The source spectrum was then measured within a circular aperture of radius 0.20 arcsec. A local background spectrum was estimated from an annulus with inner and outer radii of 0.45 and 0.95 arcsec, respectively, and subtracted from the source aperture spectrum. The same aperture geometry was also used to extract matched spectra from the PRISM cubes.

2.3. *Sample Summary*

Figure 1 summarizes the basic properties of our working sample by showing the rest-frame monochromatic luminosity at 5100 Å ($L_{5100} = \lambda L_\lambda(5100\text{Å})$) as a function of spectroscopic redshift. We classify each target as an LRD or a non-LRD based on a photometric classification of

$$\begin{aligned} &\mathrm{F277W} - \mathrm{F444W} > 1.0 \\ \wedge\ &\mathrm{F150W} - \mathrm{F200W} < 1.0 \quad (z < 4), \\ &\mathrm{F277W} - \mathrm{F444W} > 1.0 \\ \wedge\ &\mathrm{F150W} - \mathrm{F200W} < 1.0 \quad (4 < z < 6), \\ &\mathrm{F277W} - \mathrm{F444W} > 1.0 \\ \wedge\ &\mathrm{F150W} - \mathrm{F200W} < 1.0 \quad (z > 6). \end{aligned} \tag{2}$$

The criteria for $z > 6$ objects are slightly tighter ones than those suggested by P. Rinaldi et al. (2026), and the lower-redshift criteria are similarly defined to select LRDs at $z < 6$. For the photometric selection, we create pseudo photometry from the PRISM spectra. After the pseudo-photometric selection, we visually inspect the PRISM spectra to ensure that the red optical color is not mimicked by the strong emission lines. Our sample eventually comprises of 37 LRDs and 23 non-LRDs. Both the LRD and non-LRD subsamples span a comparable redshift range of $z_{\rm spec} = 3$–7. Although our sample is not statistically complete, our sample selection is free from contamination by strong emission lines and is based on broad-line characteristics, compactness, and continuum-shape criteria. These criteria effectively capture the principal spectral and morphological properties of LRDs or broad-line type 1 AGNs, yielding a high-purity sample rather than a complete one. Tables 1 and 2 summarize the basic information of the sample.

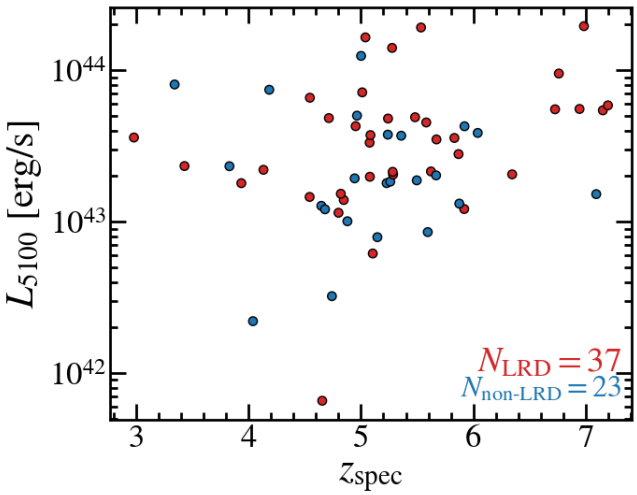

Figure 1. Rest-frame 5100 Å monochromatic luminosity as a function of spectroscopic redshift for our LRD sample. The red and blue points show the objects classified as LRDs and non-LRDs, respectively.

UNCOVER-13821 and UNCOVER-4286 are gravitationally lensed by the Abell2744 galaxy cluster. For these objects, graviational lensing magnification factors are taken from the UNCOVER magnification catalog v2.0 (L. J. Furtak et al. 2023; S. H. Price et al. 2025; K. A. Suess et al. 2024; J. R. Weaver et al. 2024). Magnification factors applied for UNCOVER-13821 and UNCOVER-4286 are $\mu = 1.6210^{+0.0053}_{-0.0148}$ and $1.607^{+0.005}_{-0.011}$, respectively.

3. ANALYSIS

3.1. *Line Profile Fitting*

Using grating spectra, we fit the Hα+[N II] complex in the DJA and NIRSpec/IFU samples. If the Hα line is covered by both medium- and high-resolution grating, we use high-resolution one. We fit the Hα+[N II] complex with the following components:

- Narrow emission component: a single Gaussian with FWHM $< 500\,\mathrm{km\,s^{-1}}$.
- Broad emission component: an exponential profile with an FWHM broader than the narrow Gaussian. The adoption of an exponential profile is motivated by several recent studies, which demonstrate that most high–signal-to-noise LRDs are better described by an exponential rather than a Gaussian profile (e.g., V. Rusakov et al. 2026; J. Scholtz et al. 2026).
- [N II] $\lambda\lambda 6548, 6583$: each line is modeled as a single Gaussian, with the line ratio fixed to the theoretical value of 2.94 (M. E. Galavis et al. 1997).

Table 1. LRDs in this study

ID	Program	RA	Dec	$z_{\rm spec}$	$L_{\rm H\alpha,broad}$	$L_{\rm H\beta,broad}$	L_{5100}	$L_{\rm bol}$
					$(10^{42}\,{\rm erg\,s^{-1}})$	$(10^{42}\,{\rm erg\,s^{-1}})$	$(10^{43}\,{\rm erg\,s^{-1}})$	$(10^{43}\,{\rm erg\,s^{-1}})$
CEERS-746	CEERS	14:19:14.19	+52:52:06.5	5.6231	$2.22^{+0.46}_{-0.32}$	···	$2.15^{+0.59}_{-0.59}$	$5.51^{+1.06}_{-0.57}$
EGS-47962	GO 4106	14:19:34.20	+52:51:24.8	6.7273	$6.95^{+4.71}_{-2.16}$	···	$5.52^{+0.64}_{-0.64}$	$11.80^{+2.78}_{-2.19}$
EGS-51623	GO 4106	14:19:32.84	+52:51:19.4	4.9528	$5.76^{+2.43}_{-1.56}$	···	$4.27^{+0.24}_{-0.24}$	$6.88^{+0.11}_{-0.10}$
EGS-71365	GO 4106	14:19:34.93	+52:54:24.2	4.8004	$0.72^{+0.48}_{-0.26}$	···	$1.15^{+0.17}_{-0.17}$	$2.82^{+0.49}_{-0.16}$
JADES-GN-38147	JADES	12:37:04.96	+62:08:54.3	5.8683	$8.81^{+41.02}_{-6.93}$	···	$2.79^{+0.76}_{-0.76}$	$18.93^{+11.06}_{-5.90}$
JADES-GN-39353	JADES	12:37:10.55	+62:09:11.1	4.8468	$1.28^{+1.59}_{-0.70}$	···	$1.39^{+0.41}_{-0.41}$	$3.49^{+0.61}_{-0.56}$
JADES-GN-68797	JADES	12:36:54.99	+62:08:46.3	5.0397	$42.42^{+9.33}_{-5.32}$	$10.95^{+3.04}_{-3.03}$	$16.48^{+0.66}_{-0.66}$	$95.86^{+4.41}_{-3.55}$
JADES-GN-73488	JADES	12:36:47.38	+62:10:38.0	4.1325	$3.92^{+0.63}_{-0.50}$	···	$2.20^{+0.13}_{-0.13}$	$3.87^{+0.04}_{-0.04}$
JADES-GN-53501	JADES	12:37:10.81	+62:11:36.9	3.4299	$4.43^{+0.18}_{-0.26}$	···	$2.33^{+0.23}_{-0.23}$	$4.22^{+0.28}_{-0.22}$
JADES-GN-23367	JADES	12:36:48.28	+62:14:56.2	2.9800	$0.69^{+0.10}_{-0.08}$	···	$3.60^{+0.17}_{-0.17}$	$2.58^{+0.11}_{-0.15}$
JADES-GN-954	JADES	12:36:36.47	+62:15:34.7	6.7608	$9.49^{+4.26}_{-2.86}$	···	$9.51^{+0.87}_{-0.87}$	$15.39^{+0.63}_{-1.14}$
JADES-GS-13704	JADES	03:32:30.37	−27:49:05.1	5.9189	$1.63^{+1.27}_{-0.72}$	···	$1.21^{+0.14}_{-0.14}$	$4.13^{+0.71}_{-0.51}$
JADES-GS-13329	JADES	03:32:33.37	−27:47:04.0	3.9358	$1.39^{+0.86}_{-0.64}$	···	$1.80^{+0.34}_{-0.34}$	$2.97^{+0.17}_{-0.15}$
JADES-GS-38562	JADES	03:32:32.61	−27:52:17.9	4.8210	$2.36^{+0.93}_{-0.56}$	···	$1.53^{+0.20}_{-0.20}$	$3.90^{+0.28}_{-0.34}$
RUBIES-EGS-925921	RUBIES	14:20:18.01	+52:56:37.8	6.9448	$12.65^{+1.96}_{-1.70}$	···	$5.55^{+2.13}_{-2.13}$	$26.29^{+36.54}_{-9.84}$
RUBIES-EGS-926125	RUBIES	14:20:32.90	+52:59:18.8	5.2858	$3.99^{+0.85}_{-0.86}$	···	$2.05^{+0.49}_{-0.49}$	$5.86^{+2.87}_{-0.53}$
RUBIES-EGS-24948	RUBIES	14:19:55.52	+52:52:57.2	4.5457	$0.64^{+0.82}_{-0.51}$	···	$6.58^{+0.68}_{-0.68}$	$10.88^{+0.72}_{-0.62}$
RUBIES-EGS-29489	RUBIES	14:20:05.30	+52:55:14.8	4.5434	$2.52^{+1.20}_{-0.59}$	···	$1.46^{+0.42}_{-0.42}$	$1.96^{+0.63}_{-0.48}$
RUBIES-EGS-42046	RUBIES	14:19:10.89	+52:47:19.8	5.2772	$30.82^{+14.32}_{-12.82}$	$3.96^{+2.76}_{-2.09}$	$14.04^{+0.68}_{-0.68}$	$19.33^{+1.95}_{-2.29}$
RUBIES-EGS-55604	RUBIES	14:19:55.93	+52:57:21.6	6.9843	$55.99^{+14.37}_{-12.94}$	$8.39^{+3.61}_{-3.48}$	$19.55^{+1.86}_{-1.86}$	$36.11^{+2.70}_{-1.41}$
RUBIES-EGS-61496	RUBIES	14:19:53.39	+52:57:43.9	5.0795	$2.27^{+0.98}_{-0.77}$	···	$1.98^{+0.69}_{-0.69}$	$3.24^{+0.56}_{-0.25}$
RUBIES-EGS-952625	RUBIES	14:19:54.13	+52:55:31.0	5.1051	$0.44^{+0.84}_{-0.33}$	···	$0.62^{+0.76}_{-0.76}$	$3.20^{+0.96}_{-0.44}$
RUBIES-EGS-42803	RUBIES	14:19:43.09	+52:53:16.5	7.1522	$7.08^{+7.55}_{-3.69}$	···	$5.43^{+1.61}_{-1.61}$	$11.32^{+2.31}_{-1.57}$
RUBIES-UDS-19484	RUBIES	02:16:55.78	−05:16:50.4	4.6555	$0.73^{+0.99}_{-0.43}$	···	$0.07^{+0.48}_{-0.48}$	$3.32^{+0.32}_{-0.35}$
RUBIES-UDS-182791	RUBIES	02:16:51.32	−05:05:13.4	4.7145	$10.09^{+6.97}_{-4.67}$	···	$4.83^{+0.42}_{-0.42}$	$6.55^{+1.20}_{-0.99}$
RUBIES-UDS-970351	RUBIES	02:17:02.86	−05:06:18.7	5.2822	$2.36^{+2.36}_{-1.18}$	···	$2.13^{+0.59}_{-0.59}$	$3.38^{+0.84}_{-0.30}$
RUBIES-UDS-172350	RUBIES	02:17:28.55	−05:06:14.2	5.5810	$7.55^{+4.32}_{-3.29}$	···	$4.52^{+0.65}_{-0.65}$	$7.59^{+0.58}_{-0.63}$
RUBIES-UDS-47509	RUBIES	02:17:03.50	−05:13:57.3	5.6718	$4.48^{+0.51}_{-0.76}$	···	$3.49^{+0.82}_{-0.82}$	$8.52^{+1.40}_{-0.75}$
RUBIES-UDS-981721	RUBIES	02:17:29.37	−05:06:57.3	7.1977	$12.16^{+3.58}_{-2.60}$	···	$5.86^{+1.94}_{-1.94}$	$14.66^{+3.03}_{-4.04}$
159717	BlackThunder	03:32:23.40	−27:54:04.7	5.0775	$7.19^{+0.54}_{-0.47}$	···	$3.32^{+0.28}_{-0.28}$	$14.31^{+0.91}_{-1.04}$
UNCOVER-13821	BlackThunder	00:14:28.94	−30:24:00.0	6.3454	$5.87^{+0.58}_{-0.53}$	···	$2.05^{+1.54}_{-1.54}$	$7.56^{+0.92}_{-1.44}$
UNCOVER-4286	BlackThunder	00:14:28.61	−30:25:23.9	5.8315	$3.82^{+0.47}_{-0.47}$	···	$3.57^{+0.85}_{-0.85}$	$3.80^{+0.09}_{-0.18}$
J1148-18404	BlackThunder	11:48:13.92	+52:51:46.1	5.0115	$7.10^{+0.49}_{-0.50}$	···	$7.14^{+0.86}_{-0.86}$	$15.27^{+0.17}_{-0.12}$
GN-12839	GO 5664	12:37:22.75	+62:15:47.2	5.2411	$24.02^{+0.21}_{-0.24}$	···	$4.80^{+0.30}_{-0.30}$	$27.06^{+0.52}_{-0.54}$
GN-15498	GO 5664	12:37:08.52	+62:16:50.9	5.0846	$4.64^{+0.75}_{-0.65}$	···	$3.73^{+0.30}_{-0.30}$	$7.27^{+0.07}_{-0.04}$
GN-9771	GO 5664	12:37:07.44	+62:14:50.3	5.5346	$52.07^{+0.97}_{-1.01}$	$5.98^{+1.28}_{-0.95}$	$19.16^{+0.43}_{-0.43}$	$21.56^{+0.11}_{-0.08}$
GS-13971	GO 5664	03:32:33.26	−27:47:25.1	5.4816	$6.81^{+0.09}_{-0.10}$	···	$4.89^{+0.31}_{-0.31}$	$9.57^{+0.69}_{-0.27}$

Note—Program references: CEERS (S. L. Finkelstein et al. 2022); GO-4106 (PI: Nelson); JADES (D. J. Eisenstein et al. 2026); RUBIES (A. de Graaff et al. 2025a); BlackTHUNDER (H. Übler et al. 2025); (A. Torralba et al. 2026; J. Matthee et al. 2026).

Table 2. non-LRDs in this study

ID	Program	RA	Dec	$z_{\rm spec}$	$L_{\rm H\alpha,broad}$ ($10^{42}\,{\rm erg\,s^{-1}}$)	L_{5100} ($10^{43}\,{\rm erg\,s^{-1}}$)
JADES-GN-77652	JADES	12:37:10.37	+62:11:56.4	5.2286	$1.72^{+1.09}_{-0.56}$	$1.80^{+0.59}_{-0.59}$
JADES-GN-61888	JADES	12:36:40.32	+62:13:01.2	5.8752	$1.67^{+2.29}_{-1.27}$	$1.32^{+0.33}_{-0.33}$
JADES-GN-1093	JADES	12:36:43.14	+62:13:28.7	5.5944	$1.21^{+2.80}_{-0.87}$	$0.85^{+0.37}_{-0.37}$
JADES-GN-20621	JADES	12:36:29.40	+62:17:34.3	4.6802	$1.25^{+17.02}_{-1.19}$	$1.21^{+0.46}_{-0.46}$
JADES-GN-1121	JADES	12:36:31.16	+62:16:52.2	3.3420	$1.25^{+11.36}_{-1.13}$	$8.05^{+0.21}_{-0.21}$
JADES-GS-9515	JADES	03:32:31.88	−27:48:06.7	4.6477	$1.32^{+0.11}_{-0.09}$	$1.27^{+0.08}_{-0.08}$
JADES-GS-13520	JADES	03:32:31.58	−27:48:35.6	4.9441	$1.12^{+1.09}_{-0.62}$	$1.93^{+0.26}_{-0.26}$
JADES-GS-10013268	JADES	03:32:48.44	−27:49:15.2	4.0395	$0.31^{+0.47}_{-0.16}$	$0.22^{+0.18}_{-0.18}$
JADES-GS-179198	JADES	03:32:21.35	−27:51:38.5	3.8299	$0.77^{+0.29}_{-0.24}$	$2.32^{+0.15}_{-0.15}$
JADES-GS-172975	JADES	03:32:21.06	−27:52:16.5	4.7417	$0.88^{+0.14}_{-0.11}$	$0.32^{+0.26}_{-0.26}$
JADES-GS-73690	JADES	03:32:14.53	−27:50:54.2	5.4967	$1.11^{+1.13}_{-0.62}$	$1.87^{+0.38}_{-0.38}$
JADES-GS-30148179	JADES	03:32:34.10	−27:46:47.5	5.9214	$2.07^{+2.56}_{-0.48}$	$4.27^{+0.47}_{-0.47}$
JADES-GS-165174	JADES	03:32:26.42	−27:53:08.7	4.1843	$2.01^{+0.20}_{-0.28}$	$7.43^{+0.13}_{-0.13}$
RUBIES-EGS-13872	RUBIES	14:20:31.90	+52:58:14.5	5.2611	$1.20^{+1.11}_{-0.56}$	$1.84^{+0.50}_{-0.50}$
RUBIES-EGS-6411	RUBIES	14:20:26.20	+52:56:23.2	4.8796	$0.55^{+2.04}_{-0.41}$	$1.01^{+0.39}_{-0.39}$
RUBIES-EGS-46985	RUBIES	14:19:13.36	+52:48:34.2	4.9649	$2.96^{+2.45}_{-1.71}$	$5.01^{+6.99}_{-6.99}$
RUBIES-EGS-50052	RUBIES	14:19:17.63	+52:49:49.0	5.2394	$2.47^{+3.29}_{-0.79}$	$3.76^{+0.41}_{-0.41}$
RUBIES-EGS-17146	RUBIES	14:19:47.88	+52:50:43.5	5.0012	$1.73^{+3.67}_{-1.27}$	$12.43^{+1.11}_{-1.11}$
RUBIES-UDS-174752	RUBIES	02:16:49.39	−05:06:01.8	6.0389	$3.51^{+3.49}_{-1.87}$	$3.86^{+0.86}_{-0.86}$
RUBIES-UDS-920396	RUBIES	02:16:59.48	−05:09:07.2	7.0935	$7.15^{+1.82}_{-1.15}$	$1.52^{+2.77}_{-2.77}$
RUBIES-UDS-19521	RUBIES	02:17:32.08	−05:17:15.8	5.6687	$1.53^{+4.25}_{-1.19}$	$2.02^{+0.83}_{-0.83}$
GN-16813	GO 5664	12:36:43.03	+62:17:33.0	5.3585	$4.87^{+0.18}_{-0.33}$	$3.70^{+0.35}_{-0.35}$
GN-14409	BlackThunder	12:36:17.30	+62:16:24.2	5.1461	$4.44^{+0.07}_{-0.08}$	$0.79^{+0.42}_{-0.42}$

Note—Program references: JADES (D. J. Eisenstein et al. 2026); RUBIES (A. de Graaff et al. 2025a); BlackTHUNDER (H. Übler et al. 2025); GO 5664 (A. Torralba et al. 2026; J. Matthee et al. 2026).

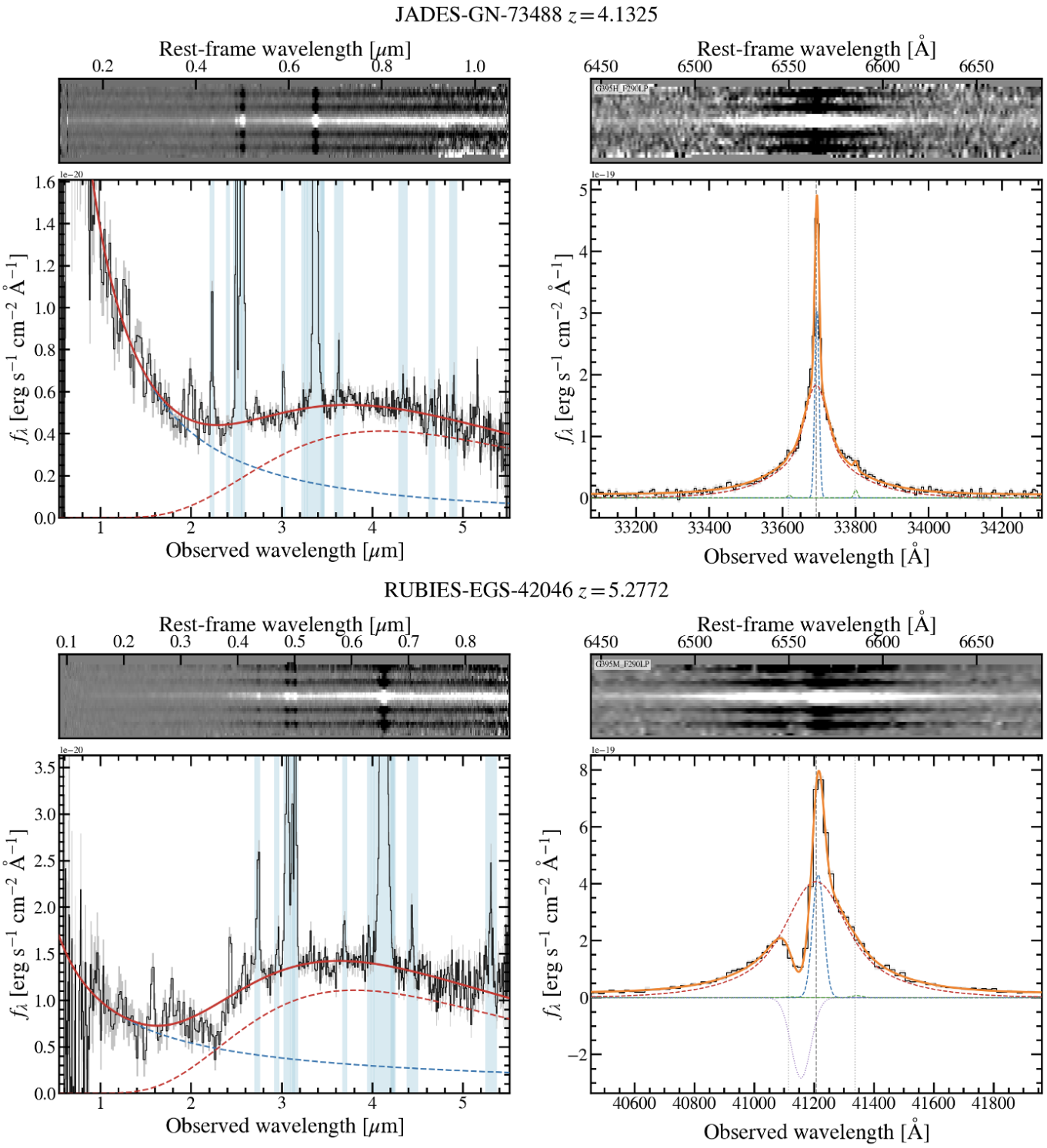

Figure 2. Representative examples of our spectral analysis. For each object (top: JADES-GN-73488; bottom: RUBIES-EGS-42046), the left panels show the NIRSpec/PRISM spectrum (black) together with the best-fit modified blackbody and power law UV continuum model (red solid curve). The red and blue dashed curves indicate the modified blackbody and power law continuum components, respectively. The blue shaded regions indicate masked intervals around emission lines. The right panels show the fit to the Hα+[N II] complex using the grating spectrum (black), decomposed into a broad component (red), narrow component (blue), [N II] lines (green), absorption line (purple), and the total model (orange) as described in Section 3.1. The vertical dotted lines show the rest-frame wavelengths of [N II]$\lambda\lambda$6548, 6583 and Hα.

- Balmer absorption (optional): we perform two fits for each object, one without absorption and one including an additional absorption component modeled as a single Gaussian.

- Continuum: a linear continuum is assumed.

We adopt a nominal rest-frame wavelength interval of 6564 ± 120 Å to ensure that the full extent of the broad emission line is encompassed by the fit. In cases where evident artifacts are present within this interval, the affected regions are excluded from the fitting range. We convolve these components with line spread functions obtained by Y. Isobe et al. (2023). When available, we also fit the Hβ emission line in the same manner, except that the [N II] doublet is not included. We infer the posterior distributions of the line-profile parameters using a Markov Chain Monte Carlo (MCMC) approach implemented with the `emcee` ensemble sampler (D. Foreman-Mackey et al. 2013). Unless otherwise stated, we adopt the 50th percentile of the marginalized posterior as the best-fit value, and the 16th and 84th percentiles as the corresponding uncertainties. To decide whether Balmer absorption is required, we fit each spectrum both with and without the absorption component and compute the Bayesian Information Criterion (BIC) for each model. We then define $\Delta\mathrm{BIC} \equiv \mathrm{BIC}_{\mathrm{no\,abs}} - \mathrm{BIC}_{\mathrm{abs}}$ and adopt the absorption-included solution when $\Delta\mathrm{BIC} > 15$; otherwise we retain the no-absorption fit. Representative examples of the fits are shown in Figure 2.

3.2. *Continuum Characterization*

We characterize the continuum shape using the JWST/NIRSpec PRISM spectra. As a first-order description, we model the continuum with a modified blackbody as done by A. de Graaff et al. (2025b):

$$f_\nu \propto B_\nu(T_{\mathrm{BB}})\,(\nu/\nu_0)^{\beta_{\mathrm{MBB}}}, \tag{3}$$

where $B_\nu(T_{\mathrm{BB}})$ is the Planck function with temperature of T_{BB}, ν_0 is the pivot frequency $\nu_0 = c/(5500\text{Å}) = 5.45 \times 10^{14}$Hz, and β_{MBB} is the power law index of modification. The adoption of a modified blackbody instead of a pure blackbody is motivated by indications of nebular continuum contributing to the optical continua of LRDs (e.g., A. Sneppen et al. 2026a). In such cases, the continuum shape could depart from that of a pure blackbody due to the contribution from the nebular continuum. However, because a detailed characterization of the physical origin of the continuum shape is beyond the scope of this study, our objective is instead to reproduce the overall spectral profile and to infer the continuum luminosity using this simplified parameterization.

Following suggestions that the rest-frame UV continuum of LRDs is spatially extended and may be dominated by host-galaxy emission rather than an unresolved central source (e.g., P. Rinaldi et al. 2025; A. P. Cloonan et al. 2026), we include an additional power-law component, $f_\lambda \propto \lambda^{\beta_{\mathrm{UV}}}$, where β_{UV} is the UV spectral slope. We then fit the modified-blackbody and power-law components simultaneously to the full PRISM spectrum. We mask wavelength intervals around prominent emission lines (Hγ, He II λ4686, Hβ, [O III]$\lambda\lambda$4959,5007, He I λ5876, [O I]$\lambda\lambda$6300,6364, Hα, [N II]$\lambda\lambda$6548, 6583, [S II]$\lambda\lambda$6718,6732, and He I λ7065) so that the inferred continuum parameters are not biased by line flux. We do not perform continuum fitting for the non-LRD sample because their optical continua are not adequately described by the modified blackbody model. Instead, for non-LRDs we only use L_{5100}.

4. RESULTS

The top-left panel of Figure 3 presents the empirical relation between the broad Hα luminosity, $L_{\mathrm{H}\alpha,\mathrm{broad}}$, and L_{5100}. We identify a correlation between the two quantities, and a power-law fit yields

$$\log\left(\frac{L_{\mathrm{H}\alpha,\mathrm{broad}}}{\mathrm{erg\,s^{-1}}}\right) = (0.91^{+0.13}_{-0.13}) \times \log\left(\frac{L_{5100}}{\mathrm{erg\,s^{-1}}}\right) - 3.2^{+5.7}_{-5.5},$$
$$\sigma_{\mathrm{int}} = 0.35^{+0.05}_{-0.04}. \tag{4}$$

The correlation between $L_{\mathrm{H}\alpha,\mathrm{broad}}$ and L_{bol} indicates that both broad line and modified-blackbody continuum are likely to be powered by the same energy source. Relative to the SDSS type 1 AGN scaling relation of J. E. Greene & L. C. Ho (2005), our best-fit relation implies that LRDs are systematically brighter in broad Hα by $\sim$0.5–1 dex at fixed L_{5100}. We also find that the non-LRD broad line AGNs lie between LRDs and low-z type 1 AGNs (J. E. Greene & L. C. Ho 2005) with larger scatters, suggesting that non-LRD broad line AGNs at high-z might be a transitioning phase from LRDs to low-z type 1 AGNs.

Because our sample requires a detected broad Hα component, the selection may preferentially include sources with larger $L_{\mathrm{H}\alpha,\mathrm{broad}}$, potentially enhancing the observed offset from the low-z type 1 AGN scaling relation. However, the offset persists even at the bright end of our sample, where incompleteness against low-$L_{\mathrm{H}\alpha,\mathrm{broad}}$ LRDs is expected to be least severe. In particular, LRDs with $L_{\mathrm{H}\alpha,\mathrm{broad}} \gtrsim 10^{43}\,\mathrm{erg\,s^{-1}}$ still lie systematically above the low-z type 1 AGN locus. Therefore, even if our broad-line selection introduces a bias in the full distribution of $L_{\mathrm{H}\alpha,\mathrm{broad}}$, the conclusion that the luminous systems exhibit an intrinsic offset is robust.

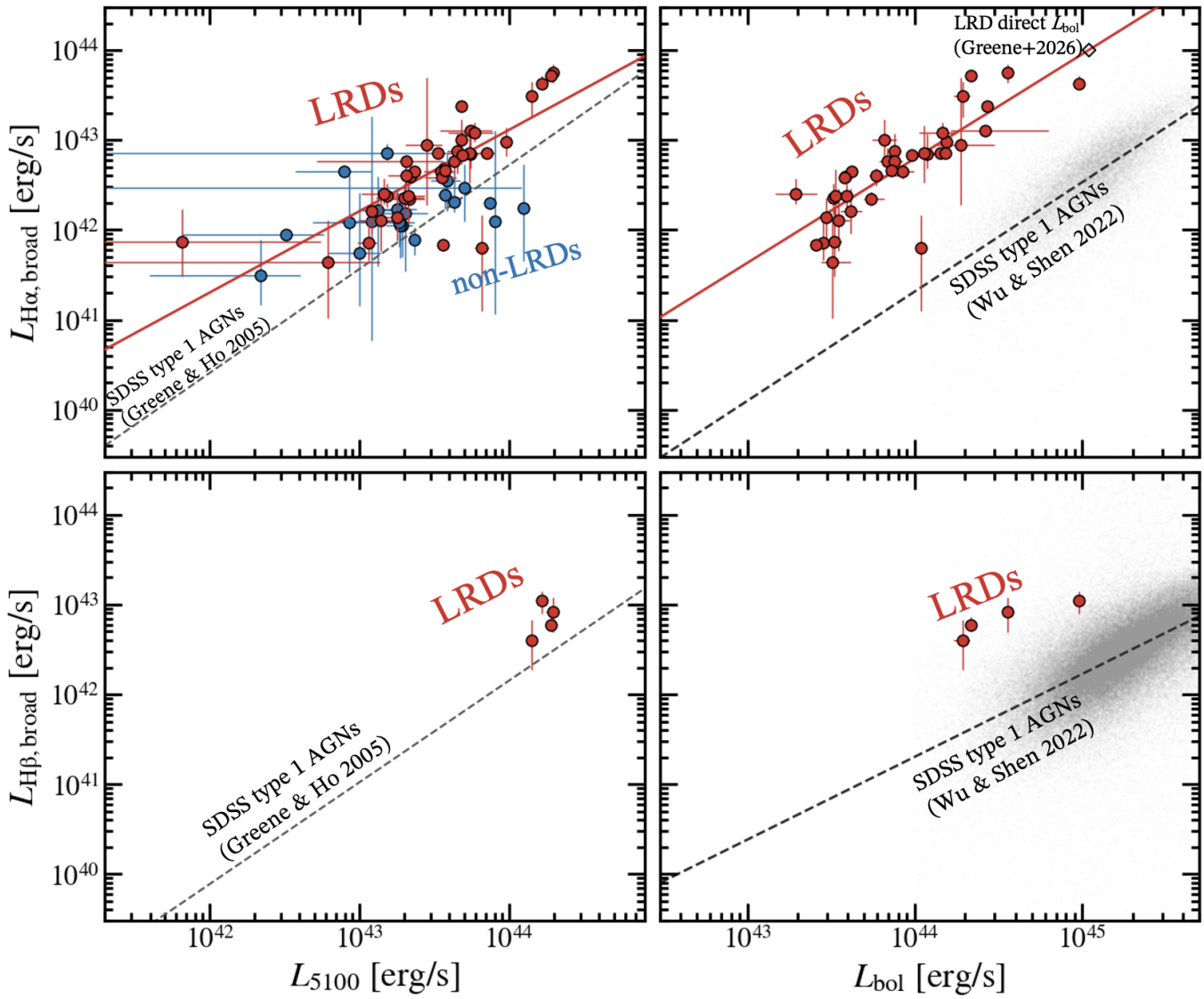

Figure 3. Scaling relations between broad Balmer line luminosities and continuum luminosities. The top and bottom rows present $L_{\rm H\alpha,broad}$ and $L_{\rm H\beta,broad}$, respectively, while the left and right column show L_{5100} and $L_{\rm bol}$, respectively. The red and blue points show luminosities of LRDs and non-LRDs measured in this work, respectively. The red solid line indicates our best-fit relation to the LRD data. The gray points and black lines show measurements and their best-fit relations for type 1 AGNs $z \lesssim 2$ from J. E. Greene & L. C. Ho (2005) (left) and Q. Wu & Y. Shen (2022) (right). The open diamond indicates the direct $L_{\rm bol}$ measurement of Abell2744-45924 (J. E. Greene et al. 2025).

In the bottom-left panel of Figure 3, we also find that four of the LRDs, which exhibit broad Hβ emission lines, show a similar yet smaller offset from the scaling relation reported by J. E. Greene & L. C. Ho (2005).

In the top-right panel of Figure 3, we additionally show the relation between $L_{\rm H\alpha,broad}$ and the bolometric luminosity, $L_{\rm bol}$, under the working assumption that the fitted modified-blackbody luminosity provides a proxy for the intrinsic bolometric output of LRDs (K. Inayoshi et al. 2025; H. Umeda et al. 2025). Under this assumption, our inferred $L_{\rm H\alpha,broad}$–$L_{\rm bol}$ relation is consistent with the direct $L_{\rm bol}$ measurements reported by J. E. Greene et al. (2025) for a luminous LRD, Abell2744-45924 (I. Labbe et al. 2024; D. J. Setton et al. 2025), constrained by broad-band observations from X-ray through far-infrared. At the same time, we find that LRDs remain offset from the SDSS type 1 AGN relation of Q. Wu & Y. Shen (2022), with broad Hα being brighter by a factor of ~ 40 at fixed $L_{\rm bol}$. We find a linear relation of

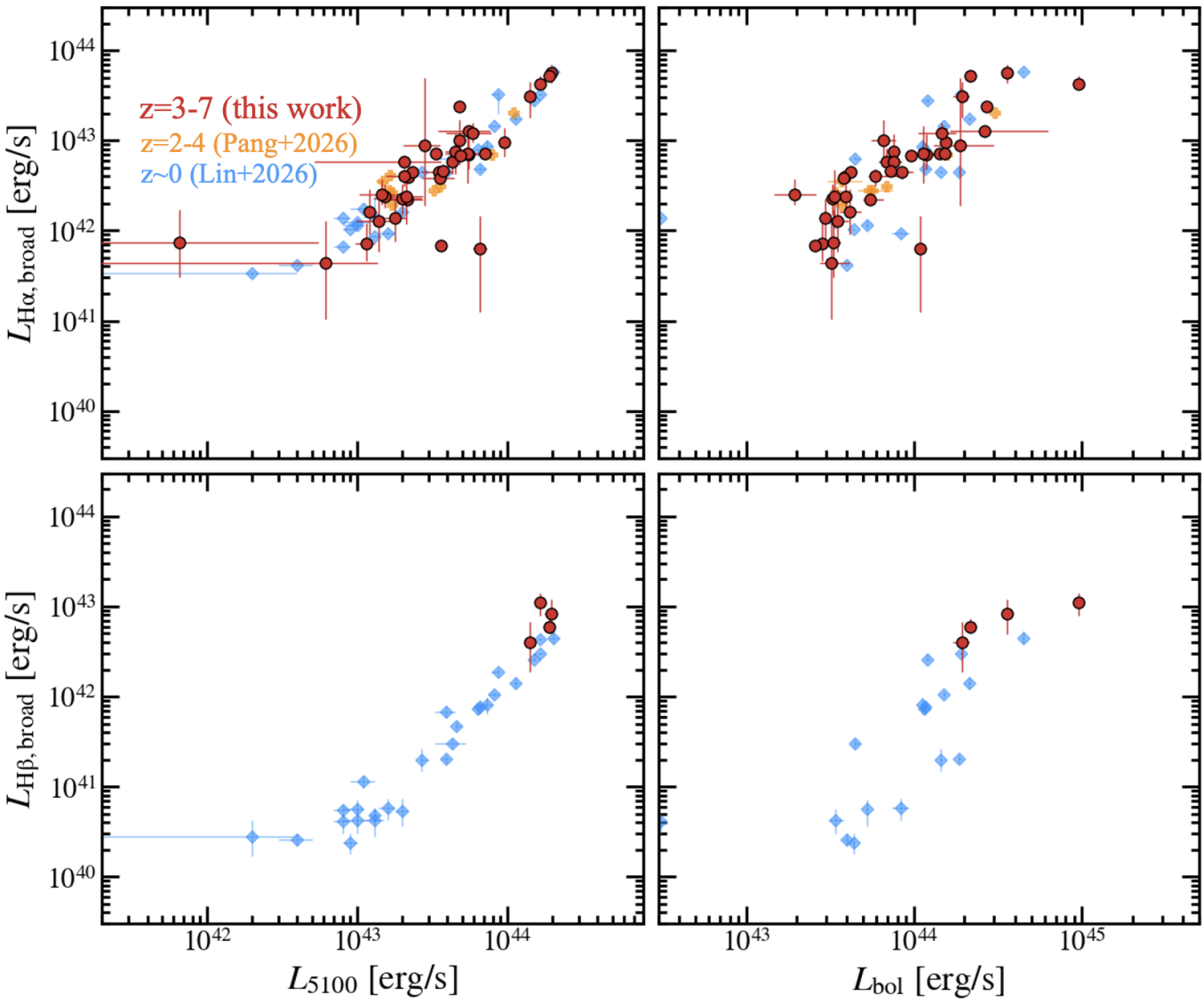

Figure 4. Same as Figure 3, but comparing the LRDs at $z = 3$–7 in this work (red circles), those at $z \sim 0$ from X. Lin et al. (2026) (blue diamonds), and those at $z \sim 2$–4 from Y. Pang et al. (2026) (orange crosses).

$$\log\left(\frac{L_{\rm H\alpha,broad}}{\rm erg\,s^{-1}}\right) = (1.2^{+0.1}_{-0.1}) \times \log\left(\frac{L_{\rm bol}}{\rm erg\,s^{-1}}\right) - 8.3^{+6.0}_{-6.0},$$
$$\sigma_{\rm int} = 0.31^{+0.04}_{-0.03}. \quad (5)$$

The broad Hβ also show the offset from the relation of Q. Wu & Y. Shen (2022), but the offset is smaller than that of Hα (by a factor of ~ 10; the bottom-right panel of Figure 3).

In Figure 4, we compare our measurements with those of $z \sim 0$ LRDs from X. Lin et al. (2026) and $z = 2$–4 LRDs from Y. Pang et al. (2026). Their lower redshift measurements fall on the same locus as our higher redshift sample, suggesting that the scaling relation of LRDs may exhibit no redshift evolution and could represent a nearly universal scaling for LRDs across cosmic time. Figure 5 further compares our measurements of total Hα luminosity, $L_{\rm H\alpha,total}$, with those of A. de Graaff et al. (2025b), which are based on the JWST/NIRSpec PRISM spectra. We find that our measurent and those of A. de Graaff et al. (2025b) are broadly consistent with each other.

5. DISCUSSIONS

5.1. *Locally Optimally-emitting Cloud (LOC) Model*

To interpret the empirical scaling relations of LRDs found in the previous section, we employ photoionization modeling. As a conceptual framework, we introduce the locally optimally-emitting cloud (LOC) model

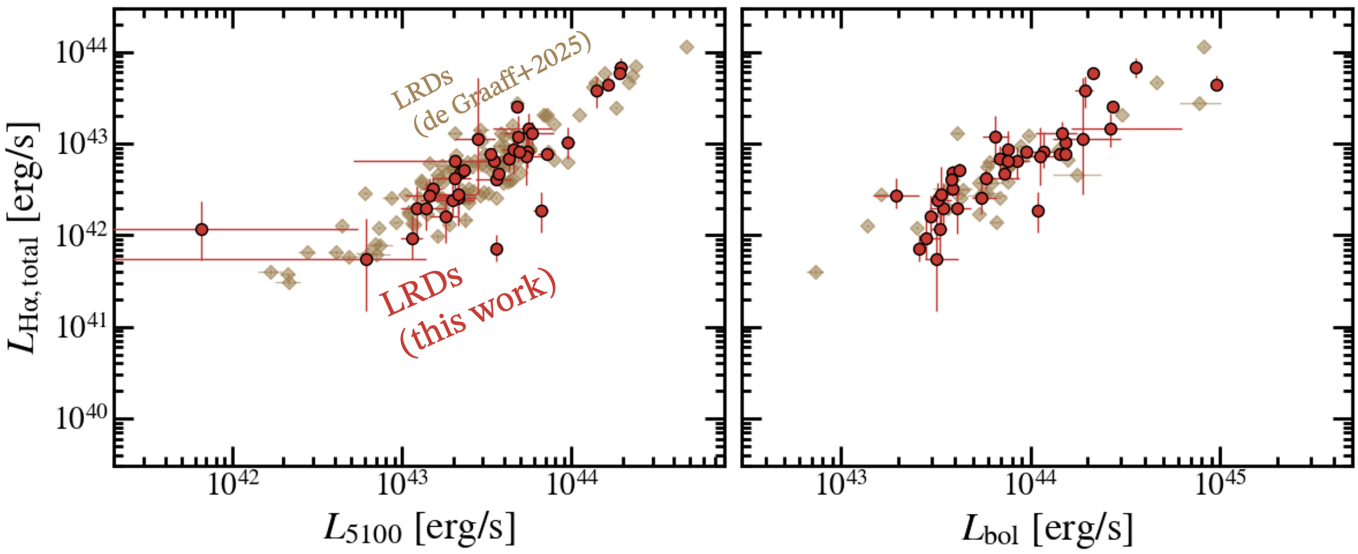

Figure 5. Same as Figure 3, but comparing the LRDs with total Hα measurements in this work (red circles) and those from A. de Graaff et al. (2025b) (brown diamonds).

(J. Baldwin et al. 1995; K. Korista et al. 1997; K. T. Korista & M. R. Goad 2004). The LOC model is a classical approach originally proposed to describe the BLR of AGNs, in which the line-emitting gas spans a broad range of hydrogen number density $n_{\rm H}$ and ionization parameter U. A key idea is that, for a given observed emission line, the emergent luminosity is dominated by the subset of clouds whose emissivity in that line is near its maximum in the $(n_{\rm H}, U)$ plane, while contributions from clouds away from the optimum conditions are subdominant. Motivated by this concept, we focus on gas conditions in the vicinity of the optimal $(n_{\rm H}, U)$ values to connect the observed $L_{\rm H\alpha,broad}$ scaling relations to the underlying ionizing continuum and BLR gas properties. Although their LOC models employ fine grids of calculations and take a weighted sum of them around the optimal gas conditions, we focus on a single $(n_{\rm H}, U)$ pair of values (i.e., one-zone model) for simplicity.

5.2. *Cloudy Setup*

We model the BLR gas with the photoionization code Cloudy version 23 (C. M. Gunasekera et al. 2023). We adopt a standard AGN ionizing spectrum normalized to a bolometric luminosity of $L_{\rm bol} = 10^{42-46}\,{\rm erg\,s^{-1}}$. Motivated by a broad line width of Balmer lines, we set a gas turbulent velocity of $300\,{\rm km\,s^{-1}}$, which is also used in Cloudy modeling of MoM-BH*1 (R. P. Naidu et al. 2025). Gas phase metallicity is set to 0.1 $Z_\odot$. Guided by the LOC arguments above, we fix the gas density and ionization parameter to $\log(n_{\rm H}/{\rm cm^{-3}}) = 10$ and $\log U = -2$, which are standard BLR parameters for the single-zone model (e.g., K. Davidson & H. Netzer 1979; B. M. Peterson 2006).

With $n_{\rm H}$ and U held fixed, changing the ionizing photon luminosity alone does not generally reproduce the enhanced Balmer-line luminosities at given $L_{\rm bol}$; instead, the Balmer-line output at a given ionizing continuum level primarily scales with the total amount of Balmer line emitting gas. We therefore treat the gas covering factor, $f_{\rm cov}$, and the hydrogen column density, $N_{\rm H}$, as free parameters that control the effective emitting area and depth of the BLR, respectively. We use a plane-parallel geometry with $f_{\rm cov} = 0.2$, which is a typical BLR gas covering factor of type 1 AGNs (e.g., J. Baldwin et al. 1995; K. T. Korista & M. R. Goad 2004), and closed geometry as a $f_{\rm cov} = 1$ case. Here we specify `sphere expanding` command in Cloudy for the closed geometry. We change $\log(N_{\rm H}/{\rm cm^{-2}})$ from 22 to 25. The Cloudy setup adopted in this work is summarized in Table 3.

5.3. *Cloudy Modeling Result: "Stuffed BLR" or "Giant BLR"?*

Figure 6 compares the observed scaling relation to the predictions of our Cloudy models. For a covering factor of $f_{\rm cov} = 0.2$, we vary the hydrogen column density from $\log(N_{\rm H}/{\rm cm^{-2}}) = 22$ to 25. Across this range, the predicted values of $L_{\rm H\alpha,broad}$ and $L_{\rm H\beta,broad}$ at a given $L_{\rm bol}$ increase only modestly, and does not reach the elevated locus occupied by LRDs. Instead, the $f_{\rm cov} = 0.2$ sequence is broadly consistent with the low-z type 1 AGN relation. In contrast, increasing the covering factor to $f_{\rm cov} = 1$ substantially boosts the Balmer-line output. In particular, models with $f_{\rm cov} = 1$ and $\log(N_{\rm H}/{\rm cm^{-2}}) \sim 24$–25 reproduce the observed LRD relation. Although $f_{\rm cov}$ and $N_{\rm H}$ are partially degener-

Table 3. Summary of the CLOUDY setup

Parameter	Value
Geometry	plane parallel ($f_{\rm cov} = 0.2$) or closed geometry ($f_{\rm cov} = 1$)
Incident radiation	AGN
$\log(L_{\rm bol}/{\rm erg\ s^{-1}})$	42–46
Turbulent velocity	$300\,{\rm km\,s^{-1}}$ (fixed)
Metallicity	0.1 $Z_\odot$ (fixed)
$\log(n_{\rm H}/{\rm cm^{-3}})$	10 (fixed)
$\log U$	-2 (fixed)
$\log(N_{\rm H}/{\rm cm^{-2}})$	22–26

ate, the observed relation requires both parameters to be extremely high. In particular, a solution with one parameter low and the other high (i.e., low-$f_{\rm cov}$/high-$N_{\rm H}$ or high-$f_{\rm cov}$/low-$N_{\rm H}$) cannot reproduce the observed locus.

In Figure 7, we demonstrate how Balmer line to bolometric luminosity ratios ($L_{\rm H\alpha,broad}/L_{\rm bol}$ and $L_{\rm H\beta,broad}/L_{\rm bol}$) depend on gas density (left), column density (center), and ionization parameter (right). We find that $L_{\rm H\alpha,broad}/L_{\rm bol}$ and $L_{\rm H\beta,broad}/L_{\rm bol}$ peaks at $\log(n_{\rm H}/{\rm cm^{-3}}) \sim 9.5$–10, $\log(N_{\rm H}/{\rm cm^{-2}}) \sim 24$–25, and $\log U \sim -2$. Together with $f_{\rm cov} \sim 1$, these parameter values reproduce the observed $L_{\rm H\alpha,broad}/L_{\rm bol}$ and $L_{\rm H\beta,broad}/L_{\rm bol}$ values for LRDs. These $n_{\rm H}$ and U values are typical for low-z type 1 AGNs (e.g., K. Davidson & H. Netzer 1979; B. M. Peterson 2006), while the $N_{\rm H}$ value preferred for LRDs are one to two orders of magnitude higher than the typical values for low-z type 1 AGNs ($\sim 10^{23}\,{\rm cm^{-2}}$; e.g., B. M. Peterson 2006). However, the $f_{\rm cov} = 0.2$ cases do not reproduce observed $L_{\rm H\alpha,broad}/L_{\rm bol}$ and $L_{\rm H\beta,broad}/L_{\rm bol}$ values for LRDs at any of $n_{\rm H}$, $N_{\rm H}$, and U values, suggesting that the high covering factor is necessary. These results demonstrate that the gas density and ionization parameter of BLR clouds in the LRDs may be common to those of low-z type 1 AGNs, while the large differences in the covering factor and column density enhance the Balmer line luminosities.

In Figure 8, we compare the mock observed spectrum predicted from our CLOUDY model with one of the LRDs in our sample, GN-9771, as an exapmle. We find that the model with $f_{\rm cov} = 1$ and $N_{\rm H} = 10^{25}\,{\rm cm^{-2}}$ yields an optical continuum similar to that observed in LRDs (note that the excess in our CLOUDY spectrum around the Balmer limit is CLOUDY artifact due to the finite number of energy levels included in the calculation; X. Ji et al. 2025; R. P. Naidu et al. 2025). This demonstrates that our model can also reproduce the overall continuum shape of LRDs.

We therefore conclude that the enhanced Balmer-line emission in LRDs can be explained, to first order, by a BLR with a high covering factor and a large gas column density. A BLR with such large $f_{\rm cov}$ and $N_{\rm H}$, while retaining standard $n_{\rm H}$ and U, suggests at least two possible scenarios (Figure 9); one is a "stuffed BLR," where the central engine is enshrouded by the BLR whose volume is filled by an extremely large number of clouds (i.e., a high volume filling factor $f_{\rm fill}$) within a radius comparable to that of normal BLRs. The other is a "giant BLR," where the central engine is covered by the BLR whose radius is substantially larger, with a $f_{\rm fill}$ value similar to that of normal BLRs. Although the BLR filling factor for the normal AGNs has poorly been constrained, $f_{\rm fill} \sim 10^{-3}$–$10^{-2}$ is typically assumed for BLRs (D. E. Osterbrock 1991; S. A. Snedden & C. M. Gaskell 1999; D. E. Osterbrock & G. J. Ferland 2006). The stuffed BLR scenario may represent a large filling factor of $f_{\rm fill} \gtrsim 10^{-2}$. On the other hand, the giant BLR may have a size one or two orders of magnitude larger than that of a typical BLR (10^{-3}–10^{-1} pc; e.g., B. M. Peterson et al. 2004; S. Kaspi et al. 2000; M. C. Bentz et al. 2013). Note that these two scenarios should be regarded as limiting cases; the true BLR configuration may be somewhere between them. These scenarios are in line with the emerging picture that LRDs host accreting black holes embedded in an optically thick, high-column-density gas cocoon (e.g., R. Maiolino et al. 2025; K. Inayoshi & R. Maiolino 2025; A. de Graaff et al. 2025c; R. P. Naidu et al. 2025; V. Rusakov et al. 2026; M. Ando et al. 2026; A. Sneppen et al. 2026b).

The stuffed BLR or giant BLR scenarios may even explain the other observations of LRDs as follows:

- Weak X-ray emission: the optically thick gas obscures the X-ray emission (e.g., T. T. Ananna et al.

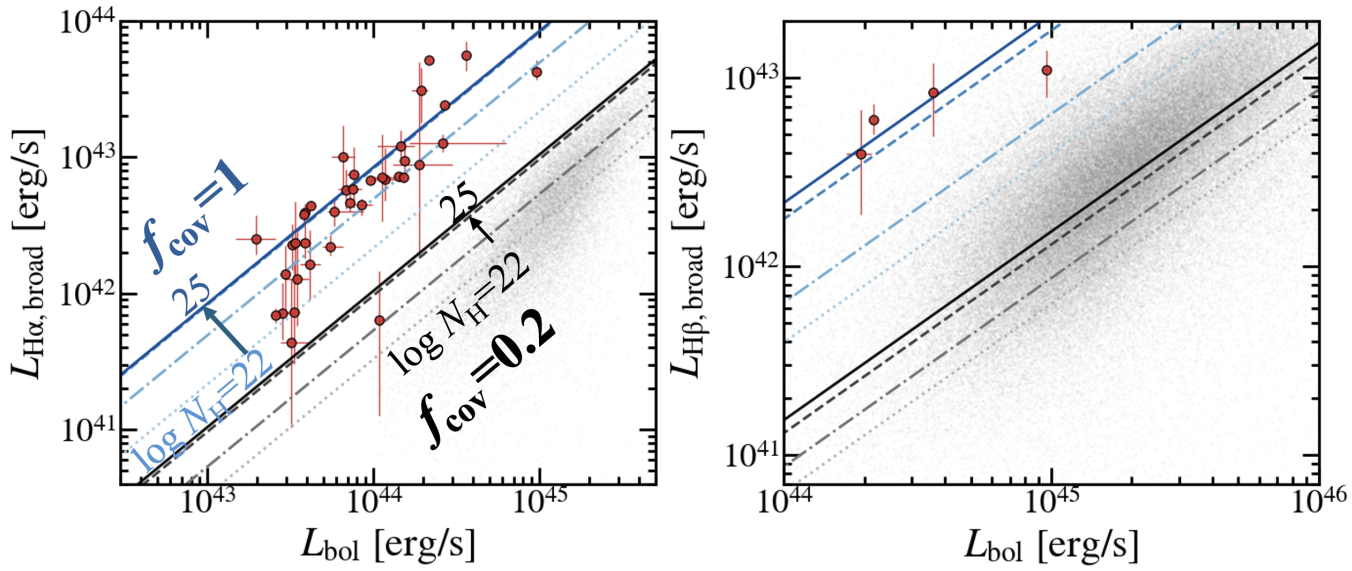

Figure 6. Comparison of the observed broad Balmer-line luminosities and bolometric luminosity with CLOUDY photoionization models. Left: $L_{\rm H\alpha,broad}$ versus $L_{\rm bol}$. Right: $L_{\rm H\beta,broad}$ versus $L_{\rm bol}$. The symbols are the same as Figures 3, 4, and 5. The gray and black lines show the models with $f_{\rm cov} = 0.2$, while the blue lines show those with $f_{\rm cov} = 1$. The dotted, dot-dashed, dashed, and solid lines correspond to $\log(N_{\rm H}/{\rm cm}^{-2}) = 22, 23, 24$, and 25, respectively.

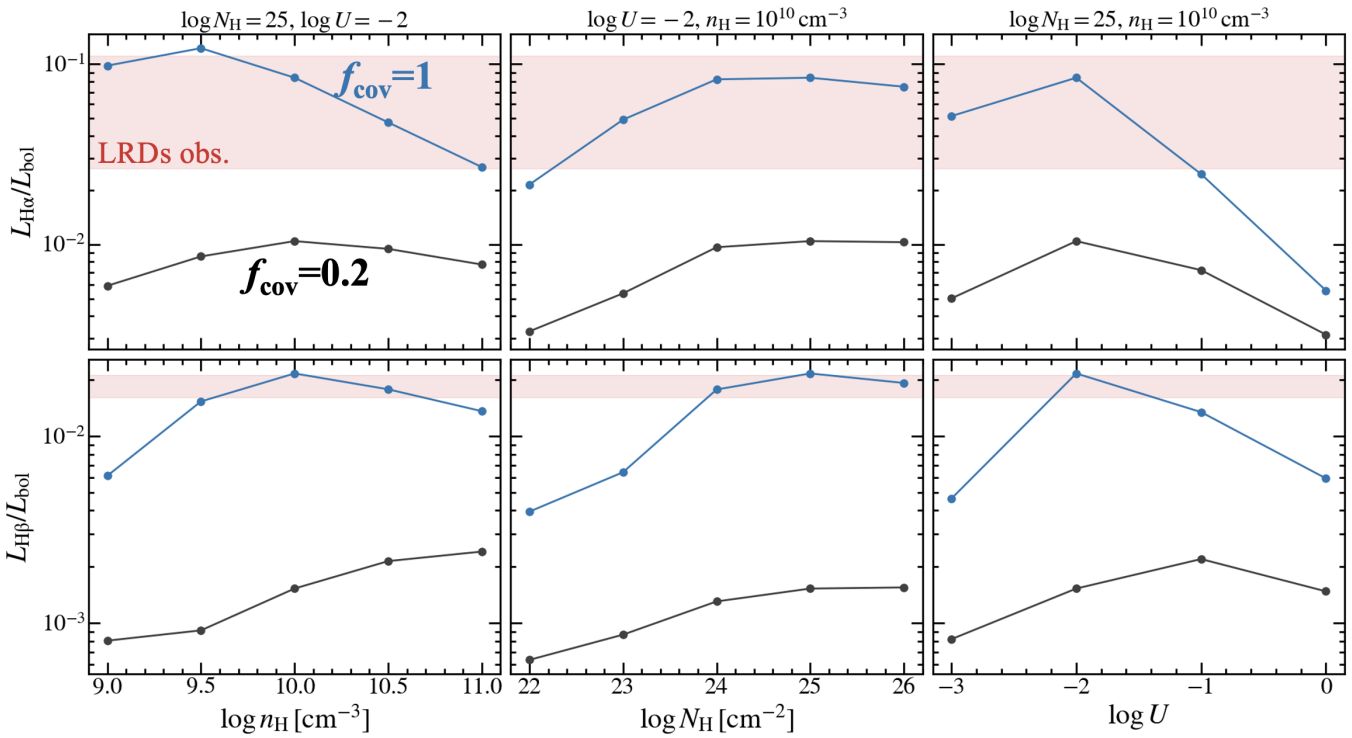

Figure 7. Broad Balmer line to bolometric luminosity ratios as functions of density (left), column density (center), and ionization parameter (right). The blue and black lines show the CLOUDY predictions of $f_{\rm cov} = 1$ and 0.2, respectively. The red shades show the 1σ ranges of the LRD sample in this work.

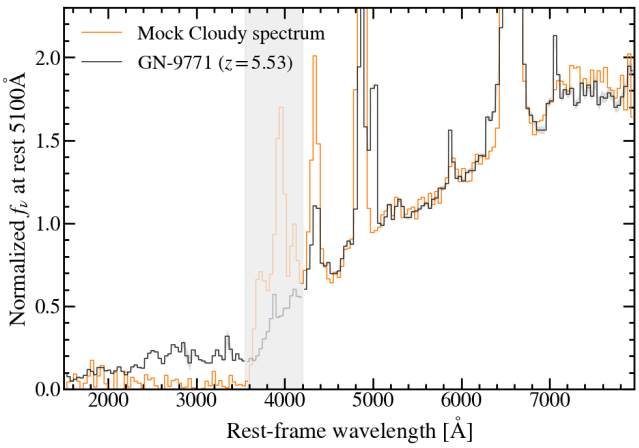

Figure 8. Mock JWST/NIRSpec PRISM spectrum generated from the CLOUDY model. The orange line shows the simulated spectrum, assuming $f_{\rm cov} = 1$, $N_{\rm H} = 10^{25}\,{\rm cm}^{-2}$, $n_{\rm H} = 10^{10}\,{\rm cm}^{-3}$, and $\log U = -2$. The black line shows the observed PRISM spectrum of the LRD in our sample GN-9771. The gray shaded region indicate the region affected by the CLOUDY artifact due to the finite number of hydrogen energy levels considered in the calculation (X. Ji et al. 2025; R. P. Naidu et al. 2025). These spectra are normalized at rest-frame 5100Å and binned in three-pixel bins to highlight the overall continuum shape.

2024; M. Yue et al. 2024; R. Maiolino et al. 2025; A. Sacchi & Á. Bogdán 2025).

- Balmer absorption lines: the optically thick gas with high density has a large column density of $n = 2$ hydrogen atoms, which causes the Balmer absorption lines (e.g., J. Matthee et al. 2024; D. D. Kocevski et al. 2025; F. D'Eugenio et al. 2026).

- Weak continuum variability of short timescale: the continuum emission may at least partially be thermalized because of the large column density. In this case, it takes a long time for continuum photons to escape from the BLR and the high frequency component of continuum variability may be blurred (A. Secunda et al. 2026), which is consistent with the weak short-term continuum variability observed in majority of LRDs (e.g., M. Kokubo & Y. Harikane 2025; Z. Zhang et al. 2025; W. L. Tee et al. 2025; Z. Stone et al. 2025; Z. Liu et al. 2026; C. J. Burke et al. 2025).

A full quantitative assessment of these points is beyond the scope of this paper and is left for future work.

6. SUMMARY

In this work, we use archival JWST/NIRSpec spectra and present statistical analysis of Balmer line and continuum luminosities of LRDs. Our analysis and results are summarized below:

- We analyze JWST/NIRSpec PRISM and grating spectra of 37 little red dots (LRDs) at $z \sim 3$–7. We decompose the Hα+[N II] complex (and Hβ where available) to isolate the broad components, and we estimate L_{5100} and an empirical $L_{\rm bol}$ from modified blackbody continuum fits to the PRISM spectra.

- We identify a tight correlation between the broad Hα luminosities and the continuum luminosities (L_{5100} and $L_{\rm bol}$). LRDs are systematically offset from the type 1 AGN scaling relations, showing ~ 40 times higher $L_{\rm H\alpha,broad}$ at fixed $L_{\rm bol}$, implying enhanced Balmer line emission efficiency.

- We interpret this offset using CLOUDY photoionization calculations within the classical LOC framework. The observed enhancement can be reproduced if LRDs have a BLR with a substantially high covering factor and large hydrogen column density than typical type 1 AGN, which simultaneously reproduce the modified blackbody continuum shape. Such gas conditions with high covering factor and large column density suggest either a very high volume filling factor or a large size of BLR, namely, "stuffed BLR" or "giant BLR," respectively.

ACKNOWLEDGMENTS

We thank Yuki Isobe for providing the line-spread functions for JWST/NIRSpec. This work is based on observations made with the NASA/ ESA/CSA James Webb Space Telescope. The NIRSpec/IFU data were obtained from the Mikulski Archive for Space Telescopes at the Space Telescope Science Institute, which is operated by the Association of Universities for Research in Astronomy, Inc., under NASA contract NAS 5-03127 for JWST. The NIRSpec MSA data presented herein were retrieved from DJA. DJA is an initiative of the Cosmic Dawn Center (DAWN), which is funded by the Danish National Research Foundation under grant DNRF140. We thank DAWN for providing the reduced NIRSpec data. The observational data presented in this work are associated with programs ERS 1345 (CEERS; PI: Finkelstein), GTO 1180 (PI: Eisenstein), GTO 1181 (PI: Eisenstein), GTO 1210 (PI: Luetzgendorf), GTO 1286 (PI: Luetzgendorf), GO 4233 (PI: de Graaff), GO 4106 (PI: Nelson), GO 5664 (PI: Matthee), GO 5015 (PI:

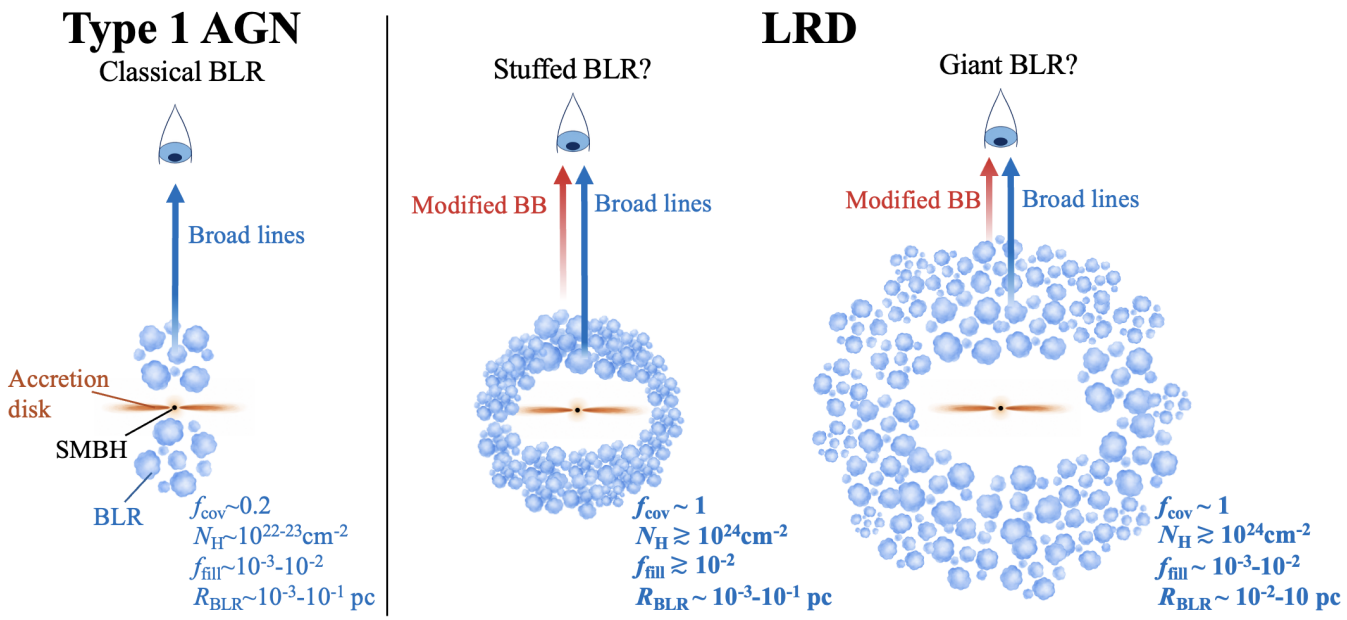

Figure 9. Schematic illustrations of the standard BLR (left), "stuffed BLR" (center), and "giant BLR" (right). The standard BLR typically have covering factor of $f_{\rm cov} \sim 0.2$ (e.g., J. Baldwin et al. 1995; K. T. Korista & M. R. Goad 2004) and column density of $\log(N_{\rm H}/{\rm cm}^{-2}) = 22$–$23$ (e.g., B. M. Peterson 2006), while our CLOUDY modeling suggests that the BLR of the LRDs have very high covering factor (almost unity) and large column density ($\log(N_{\rm H}/{\rm cm}^{-2}) \gtrsim 25$). The extremely large column density can be explained either by high filling factor (stuffed BLR) or by large BLR size (giant BLR). Either the stuffed BLR or giant BLR enhances the Balmer line emission (Figure 6) and produces the red optical continuum (Figure 8).

Übler and Maiolino), and GO 1287 (PI: Isaak). The authors acknowledge the teams conducting these observations for publicly releasing the data. HY acknowledges support by KAKENHI (25KJ0832) through Japan Society for the Promotion of Science (JSPS). MO acknowledges the supports from the World Premier International Research Center Initiative (WPI Initiative), MEXT, Japan, the joint research program of the Institute for Cosmic Ray Research (ICRR), the University of Tokyo, and KAKENHI (21H04467, 25H00674) through Japan Society for the Promotion of Science (JSPS). YK acknowledges support by KAKENHI (26KJ0960) through JSPS, JSR Fellowship, and FoPM, WINGS Program, the University of Tokyo. TK acknowledges support by KAKENHI (26KJ1232) through Japan Society for the Promotion of Science (JSPS). MN is supported by JSPS KAKENHI Grant Nos. 25KJ0828. The authors acknowledge the use of ChatGPT (OpenAI, GPT-5.5) and Codex (OpenAI, Codex 5.4) to assist with language editing, code development, and figure generation. All AI-assisted outputs were carefully reviewed and validated by the authors. The authors take full responsibility for all analyses, interpretations, and conclusions presented in this work.

Facilities: JWST

Software: grizli (G. Brammer 2023a,b), emcee (D. Foreman-Mackey et al. 2013), Cloudy (C. M. Gunasekera et al. 2023), Matplotlib (J. D. Hunter 2007), Astropy (Astropy Collaboration et al. 2013, 2018, 2022), NumPy (C. R. Harris et al. 2020)

REFERENCES

Akins, H. B., Casey, C. M., Lambrides, E., et al. 2025, ApJ, 991, 37, doi: 10.3847/1538-4357/ade984

Ananna, T. T., Bogdán, Á., Kovács, O. E., Natarajan, P., & Hickox, R. C. 2024, ApJL, 969, L18, doi: 10.3847/2041-8213/ad5669

Ando, M., Harikane, Y., Katz, H., Inayoshi, K., & Tanaka, T. S. 2026, arXiv e-prints, arXiv:2606.03522. https://arxiv.org/abs/2606.03522

Astropy Collaboration, Robitaille, T. P., Tollerud, E. J., et al. 2013, A&A, 558, A33, doi: 10.1051/0004-6361/201322068

Astropy Collaboration, Price-Whelan, A. M., Sipőcz, B. M., et al. 2018, AJ, 156, 123, doi: 10.3847/1538-3881/aabc4f
Astropy Collaboration, Price-Whelan, A. M., Lim, P. L., et al. 2022, ApJ, 935, 167, doi: 10.3847/1538-4357/ac7c74
Baldwin, J., Ferland, G., Korista, K., & Verner, D. 1995, ApJL, 455, L119, doi: 10.1086/309827
Bentz, M. C., Denney, K. D., Grier, C. J., et al. 2013, ApJ, 767, 149, doi: 10.1088/0004-637X/767/2/149
Brammer, G. 2023a, grizli, 1.9.11 Zenodo, doi: 10.5281/zenodo.1146904
Brammer, G. 2023b, grizli, 1.9.11 Zenodo, doi: 10.5281/zenodo.8370018
Burke, C. J., Stone, Z., Shen, Y., & Jiang, Y.-F. 2025, arXiv e-prints, arXiv:2511.16082, doi: 10.48550/arXiv.2511.16082
Cloonan, A. P., Whitaker, K. E., Manning, S. M., et al. 2026, arXiv e-prints, arXiv:2603.24700, doi: 10.48550/arXiv.2603.24700
Davidson, K., & Netzer, H. 1979, Reviews of Modern Physics, 51, 715, doi: 10.1103/RevModPhys.51.715
de Graaff, A., Brammer, G., Weibel, A., et al. 2025a, A&A, 697, A189, doi: 10.1051/0004-6361/202452186
de Graaff, A., Hviding, R. E., Naidu, R. P., et al. 2025b, arXiv e-prints, arXiv:2511.21820, doi: 10.48550/arXiv.2511.21820
de Graaff, A., Rix, H.-W., Naidu, R. P., et al. 2025c, A&A, 701, A168, doi: 10.1051/0004-6361/202554681
D'Eugenio, F., Juodžbalis, I., Ji, X., et al. 2026, MNRAS, 545, staf2117, doi: 10.1093/mnras/staf2117
Eisenstein, D. J., Willott, C., Alberts, S., et al. 2026, ApJS, 283, 6, doi: 10.3847/1538-4365/ae3163
Finkelstein, S. L., Bagley, M. B., Arrabal Haro, P., et al. 2022, ApJL, 940, L55, doi: 10.3847/2041-8213/ac966e
Foreman-Mackey, D., Hogg, D. W., Lang, D., & Goodman, J. 2013, PASP, 125, 306, doi: 10.1086/670067
Furtak, L. J., Zitrin, A., Weaver, J. R., et al. 2023, MNRAS, 523, 4568, doi: 10.1093/mnras/stad1627
Galavis, M. E., Mendoza, C., & Zeippen, C. J. 1997, A&AS, 123, 159, doi: 10.1051/aas:1997344
Gloudemans, A. J., Duncan, K. J., Eilers, A.-C., et al. 2025, ApJ, 986, 130, doi: 10.3847/1538-4357/adddb9
Greene, J. E., & Ho, L. C. 2005, ApJ, 630, 122, doi: 10.1086/431897
Greene, J. E., Labbe, I., Goulding, A. D., et al. 2024, ApJ, 964, 39, doi: 10.3847/1538-4357/ad1e5f
Greene, J. E., Setton, D. J., Furtak, L. J., et al. 2025, arXiv e-prints, arXiv:2509.05434, doi: 10.48550/arXiv.2509.05434
Gunasekera, C. M., van Hoof, P. A. M., Chatzikos, M., & Ferland, G. J. 2023, Research Notes of the American Astronomical Society, 7, 246, doi: 10.3847/2515-5172/ad0e75
Harikane, Y., Zhang, Y., Nakajima, K., et al. 2023, ApJ, 959, 39, doi: 10.3847/1538-4357/ad029e
Harris, C. R., Millman, K. J., van der Walt, S. J., et al. 2020, Nature, 585, 357, doi: 10.1038/s41586-020-2649-2
Heintz, K. E., Watson, D., Brammer, G., et al. 2024, Science, 384, 890, doi: 10.1126/science.adj0343
Hunter, J. D. 2007, Computing in Science and Engineering, 9, 90, doi: 10.1109/MCSE.2007.55
Inayoshi, K., & Ho, L. C. 2025, arXiv e-prints, arXiv:2512.03130, doi: 10.48550/arXiv.2512.03130
Inayoshi, K., & Maiolino, R. 2025, ApJL, 980, L27, doi: 10.3847/2041-8213/adaebd
Inayoshi, K., Murase, K., & Kashiyama, K. 2025, arXiv e-prints, arXiv:2509.19422, doi: 10.48550/arXiv.2509.19422
Isobe, Y., Ouchi, M., Nakajima, K., et al. 2023, ApJ, 956, 139, doi: 10.3847/1538-4357/acf376
Ji, X., Maiolino, R., Übler, H., et al. 2025, MNRAS, 544, 3900, doi: 10.1093/mnras/staf1867
Kaspi, S., Smith, P. S., Netzer, H., et al. 2000, ApJ, 533, 631, doi: 10.1086/308704
Kido, D., Ioka, K., Hotokezaka, K., Inayoshi, K., & Irwin, C. M. 2025, MNRAS, 544, 3407, doi: 10.1093/mnras/staf1898
Kiyota, T., Ouchi, M., Xu, Y., et al. 2025, ApJ, 995, 150, doi: 10.3847/1538-4357/ae1cc3
Kocevski, D. D., Onoue, M., Inayoshi, K., et al. 2023, ApJL, 954, L4, doi: 10.3847/2041-8213/ace5a0
Kocevski, D. D., Finkelstein, S. L., Barro, G., et al. 2025, ApJ, 986, 126, doi: 10.3847/1538-4357/adbc7d
Kokubo, M., & Harikane, Y. 2025, ApJ, 995, 24, doi: 10.3847/1538-4357/ae119e
Korista, K., Baldwin, J., Ferland, G., & Verner, D. 1997, ApJS, 108, 401, doi: 10.1086/312966
Korista, K. T., & Goad, M. R. 2004, ApJ, 606, 749, doi: 10.1086/383193
Labbe, I., Greene, J. E., Matthee, J., et al. 2024, arXiv e-prints, arXiv:2412.04557, doi: 10.48550/arXiv.2412.04557
Labbe, I., Greene, J. E., Bezanson, R., et al. 2025, ApJ, 978, 92, doi: 10.3847/1538-4357/ad3551
Lin, X., Fan, X., Cai, Z., et al. 2026, arXiv e-prints, arXiv:2605.21574, doi: 10.48550/arXiv.2605.21574
Liu, Z., Naidu, R. P., Secunda, A., et al. 2026, arXiv e-prints, arXiv:2604.13000, doi: 10.48550/arXiv.2604.13000

Maiolino, R., Scholtz, J., Curtis-Lake, E., et al. 2024, A&A, 691, A145, doi: 10.1051/0004-6361/202347640
Maiolino, R., Risaliti, G., Signorini, M., et al. 2025, MNRAS, 538, 1921, doi: 10.1093/mnras/staf359
Matthee, J., Naidu, R. P., Brammer, G., et al. 2024, ApJ, 963, 129, doi: 10.3847/1538-4357/ad2345
Matthee, J., Torralba, A., Pezzulli, G., et al. 2026, arXiv e-prints, arXiv:2603.17667, doi: 10.48550/arXiv.2603.17667
Naidu, R. P., Matthee, J., Katz, H., et al. 2025, arXiv e-prints, arXiv:2503.16596, doi: 10.48550/arXiv.2503.16596
Osterbrock, D. E. 1991, Reports on Progress in Physics, 54, 579, doi: 10.1088/0034-4885/54/4/002
Osterbrock, D. E., & Ferland, G. J. 2006, Astrophysics of gaseous nebulae and active galactic nuclei
Pang, Y., Wang, X., Cheng, C., et al. 2026, arXiv e-prints, arXiv:2602.12548, doi: 10.48550/arXiv.2602.12548
Peterson, B. M. 2006, in Physics of Active Galactic Nuclei at all Scales, ed. D. Alloin, Vol. 693, 77, doi: 10.1007/3-540-34621-X_3
Peterson, B. M., Ferrarese, L., Gilbert, K. M., et al. 2004, ApJ, 613, 682, doi: 10.1086/423269
Planck Collaboration, Aghanim, N., Akrami, Y., et al. 2020, A&A, 641, A6, doi: 10.1051/0004-6361/201833910
Price, S. H., Bezanson, R., Labbe, I., et al. 2025, ApJ, 982, 51, doi: 10.3847/1538-4357/adaec1
Rinaldi, P., Bonaventura, N., Rieke, G. H., et al. 2025, ApJ, 992, 71, doi: 10.3847/1538-4357/adfa10
Rinaldi, P., Hainline, K., D'Eugenio, F., et al. 2026, arXiv e-prints, arXiv:2604.07138, doi: 10.48550/arXiv.2604.07138
Rusakov, V., Watson, D., Nikopoulos, G. P., et al. 2026, Nature, 649, 574, doi: 10.1038/s41586-025-08643-8
Sacchi, A., & Bogdán, Á. 2025, ApJL, 989, L30, doi: 10.3847/2041-8213/adf5c8
Scholtz, J., D'Eugenio, F., Maiolino, R., et al. 2026, arXiv e-prints, arXiv:2603.22277, doi: 10.48550/arXiv.2603.22277
Secunda, A., Somerville, R. S., Jiang, Y.-F., et al. 2026, ApJ, 996, 6, doi: 10.3847/1538-4357/ae1f08
Setton, D. J., Greene, J. E., Spilker, J. S., et al. 2025, ApJL, 991, L10, doi: 10.3847/2041-8213/ade78b
Shen, Y., & Liu, X. 2012, ApJ, 753, 125, doi: 10.1088/0004-637X/753/2/125
Snedden, S. A., & Gaskell, C. M. 1999, ApJL, 521, L91, doi: 10.1086/312188
Sneppen, A., Matthews, J. H., Watson, D., et al. 2026a, arXiv e-prints, arXiv:2604.09399, doi: 10.48550/arXiv.2604.09399
Sneppen, A., Watson, D., Matthews, J. H., et al. 2026b, arXiv e-prints, arXiv:2601.18864, doi: 10.48550/arXiv.2601.18864
Stern, J., & Laor, A. 2012, Monthly Notices of the Royal Astronomical Society, 423, 600, doi: 10.1111/j.1365-2966.2012.20901.x
Stone, Z., Shen, Y., Zhuang, M.-Y., et al. 2025, arXiv e-prints, arXiv:2509.19585, doi: 10.48550/arXiv.2509.19585
Suess, K. A., Weaver, J. R., Price, S. H., et al. 2024, ApJ, 976, 101, doi: 10.3847/1538-4357/ad75fe
Tanaka, T. S., Akins, H. B., Harikane, Y., et al. 2025, ApJ, 995, 21, doi: 10.3847/1538-4357/ae145f
Tee, W. L., Fan, X., Wang, F., & Yang, J. 2025, ApJL, 983, L26, doi: 10.3847/2041-8213/adc5e3
Torralba, A., Matthee, J., Pezzulli, G., et al. 2026, A&A, 707, A75, doi: 10.1051/0004-6361/202557537
Übler, H., Mazzolari, G., Maiolino, R., et al. 2025, arXiv e-prints, arXiv:2509.21575, doi: 10.48550/arXiv.2509.21575
Umeda, H., Inayoshi, K., Harikane, Y., & Murase, K. 2025, arXiv e-prints, arXiv:2512.04208, doi: 10.48550/arXiv.2512.04208
Valentino, F., Brammer, G., Gould, K. M. L., et al. 2023, ApJ, 947, 20, doi: 10.3847/1538-4357/acbefa
Valentino, F., Heintz, K. E., Brammer, G., et al. 2025, A&A, 699, A358, doi: 10.1051/0004-6361/202553908
Weaver, J. R., Cutler, S. E., Pan, R., et al. 2024, ApJS, 270, 7, doi: 10.3847/1538-4365/ad07e0
Wu, Q., & Shen, Y. 2022, ApJS, 263, 42, doi: 10.3847/1538-4365/ac9ead
Yue, M., Eilers, A.-C., Ananna, T. T., et al. 2024, ApJL, 974, L26, doi: 10.3847/2041-8213/ad7eba
Zhang, Z., Jiang, L., Liu, W., & Ho, L. C. 2025, ApJ, 985, 119, doi: 10.3847/1538-4357/adcb3e